*Journal of Chromatography*, 239 (1982) 397–410
Elsevier Scientific Publishing Company, Amsterdam — Printed in The Netherlands

CHROM. 14,594

# SPACIAL DISTRIBUTION OF IONS AND ELECTRONS WITHIN $^{63}$Ni IONIZATION CELLS

E. P. GRIMSRUD* and M. J. CONNOLLY
*Department of Chemistry, Montana State University, Bozeman, MT 59717 (U.S.A.)*

## SUMMARY

Measurements of ion densities within a specialized $^{63}$Ni ionization cell are described where the distance between a radioactive foil and the point of ion density measurement is continuously variable. Air and dichlorodifluoromethane are used as the ionizing medium. Measurements are made with an atmospheric pressure ionization mass spectrometer. The results are shown to be in excellent agreement with a simple quantitative model of the experiment. The model is then used to predict the distribution of ions throughout the active volumes of several cylindrical cells of typical dimensions.

## INTRODUCTION

Radioactive beta emitters have become integral components of several important detectors for gas chromatography (GC). The electron-capture detector (ECD) is the most established among these, while the relatively newer techniques of ion mobility spectrometry (IMS) and atmospheric pressure ionization mass spectrometry (APIMS) show considerable promise. In the future development of instruments which require ionization of gases at relatively high pressures, we might expect to find beta emitters fulfilling that function.

An important characteristic of each beta source which we wish to explore here relates to their penetration into a gas and the subsequent distribution of ions and electrons throughout an ionization cell. The nature of beta penetration into GC carrier gases has been a point of continuous interest since the first uses of radiation sources for GC detection. From the known, maximum energies associated with the various beta-emitting nuclides, estimates of the "maximum" or "average" penetration depths have been made and, for the lack of more complete information, have been used as criteria for cell design. A complete description of the ionization caused by a given source is complicated by at least the following realities: a beta emitter produces beta particles of a broad range of energies; the trajectory of a beta particle through an absorbing medium is not necessarily straight; the material onto which the beta nuclide is plated will affect the energy distribution of the emitted betas due to backscattering; and the design of the cell strongly affects the net distribution of radiation and ionization. Due to these complexities, perhaps the most reliable infor-

0021-9673/82/0000–0000/$02.75 

mation concerning GC beta sources obtained so far has been by measurements of cell currents under actual or simulated conditions of the ionization cell of interest. Recently, separate reports by Aue and Kapila[1] and by Ayala *et al.*[2] have described experiments in which the standing currents observed in $^{63}$Ni and $^{3}$H ionization cells are interpreted in terms of the probable penetration depths of the betas. Such measurements of cell current reflect an integration or sum of all ionization events occurring everywhere in the cell being examined.

The measurements to be reported here offer additional and complementary information to the subject of beta penetration into a gas in that they reflect the ion density at a specific location in an ionization cell, rather than the total cell current. An advantage of this approach is that the results obtained with our specialized cell are directly transformable to other source designs. Therefore, in this article we will describe and present evidence supporting a simple quantitative model by which radiation intensity and ion densities throughout any imagined cell can be predicted with much greater accuracy than has been previously possible. Because of its wide use in ionization cells, $^{63}$Ni-on-Pt foil is the subject of this study. The method developed here for predicting the character of an ionization cell can be applied to any beta source other than $^{63}$Ni, as long as the mass absorption curve of the source material is known.

## EXPERIMENTAL

The APIMS system used in this study has been described previously[3,4]. Two slightly different ion source configurations have been used here. These are shown in Fig. 1. In ion source A of Fig. 1, the only piece of $^{63}$Ni-on-Pt foil present is a small disk of 3.0 mm diameter and 0.20 mCi activity. It is held onto the end of a moveable pin as shown. A stainless-steel cap holds the $^{63}$Ni disk in place by overlapping it slightly, so that the effective, exposed portion of the disk is then 2.8 mm in diameter. Carrier gas is passed through the source from right to left as shown in the figure at a flow-rate of *ca.* 30 ml min$^{-1}$. The right-side wall of the source is formed by a 5/8-in.

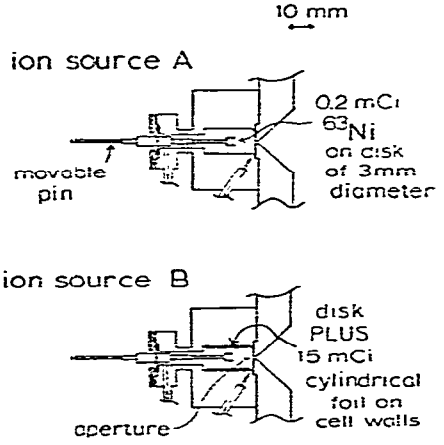


Fig. 1. Specialized atmospheric pressure ion sources in which the distance between a $^{63}$Ni-on-Pt disk and the ion-sampling aperture is variable.

disk of 25-$\mu$m thick nickel with a 25-$\mu$m diameter aperture in the center. This aperture allows about 5 ml atm min$^{-1}$ of the source contents to enter a vacuum envelope. The ion content of this gas is monitored by a quadrupole mass filter with an ion-counting detection system. In the measurements reported here, the total positive-ion signal is measured as a function of the distance between the sampling aperture and the $^{63}$Ni disk on the moveable pin. For all mass spectrometry measurements, the stainless central pin is electrically grounded to the mass spectrometer ion source so that the active volume is free of applied electrical fields at all times.

Ion source B is the same one shown as source A except that the cylindrical walls of the source now are formed by a $^{63}$Ni-on-Pt foil of 15 mCi activity. The cylinder is 10 mm in diameter and 18 mm in length. The moveable $^{63}$Ni disk is also present in source B. The activity per unit area of the two pieces of foil present in source B is the same.

For both sources the disk-to-aperture distance was continuously variable from 0.5 mm to 22 mm. The lower limit was somewhat arbitrarily decided upon so that the $^{63}$Ni disk would never come in direct contact with the gas-sampling aperture and, thereby, possibly dislodge the $^{63}$Ni disk from the pin. The moveable pin can be electrically isolated from the cell block so that the cell current can be measured (as is done in one experiment here) by using the pin as an anode. Both ion sources A and B are home-built from stainless steel.

The carrier gases used are utility-grade air and $CF_2Cl_2$. The simultaneous presence of negative ions with positive ions was actually desirable in these experiments because better reproducibility is obtained than when purified nitrogen is used. We believe that differences in reproducibility are due to the presence of small potentials which can develop on all surfaces of the cell including areas near the ion-sampling aperture. Because the diffusion velocities of positive ions and negative ions are very similar, their rates of transport to surfaces are undoubtedly nearly equivalent in the absence of applied fields and, thus, these surface potentials do not tend to occur when air is used as the source gas. Electrons, however, having a much greater diffusion velocity, may tend to cause an unequal arrival rate of the two charge types at cell boundaries when nitrogen is used. Thus, even in a perfectly clean cell, small but significant equilibrium potentials can exist at the cell boundaries. This effect is magnified if the cell is not perfectly clean (the usual case). Then a thin layer of matter separates the point of contact of the ion or electron with the conducting walls and additional boundary potentials can be created. Since the penetration depths of the betas are determined only by the mass density of the attenuating medium, and not at all affected by the ultimate fate of the negative portion of the charge pairs created, we have used gases in which negative ions will be formed.

## RESULTS AND DISCUSSION

The principle experimental results to be considered in this paper are shown in Fig. 2. The total positive-ion signal of the mass spectrometer is shown as a function of the disk-to-aperture distance, $d$, where air and $CF_2Cl_2$ were used as the carrier gas with source A and air with source B. Fig. 2 shows that each of the three experiments produced a dependence of signal on $d$ which is unique and distinct from the other two. Of the three sets of data shown, only the magnitudes of the two sets of air

measurements can be meaningfully compared with each other, since only for these two sets could the mass spectrometer ion focusing and detector settings be unchanged without exceeding the dynamic response range of the instrument. The relative magnitude of the $CF_2Cl_2$ data at any value of $d$ cannot be meaningfully compared with the air data, however, because very different mass spectrometer focusing settings where required with $CF_2Cl_2$ in order to keep the measurements at low disk-to-aperture distances within the dynamic response range of the instrument. Thus, in comparing the measurement of $CF_2Cl_2$ with those of air using source A, only the relative shapes of the two curves should be considered, and they are, indeed, seen to be distinguishably different. The $CF_2Cl_2$ data increases much more sharply as $d$ is made small than does the air data.

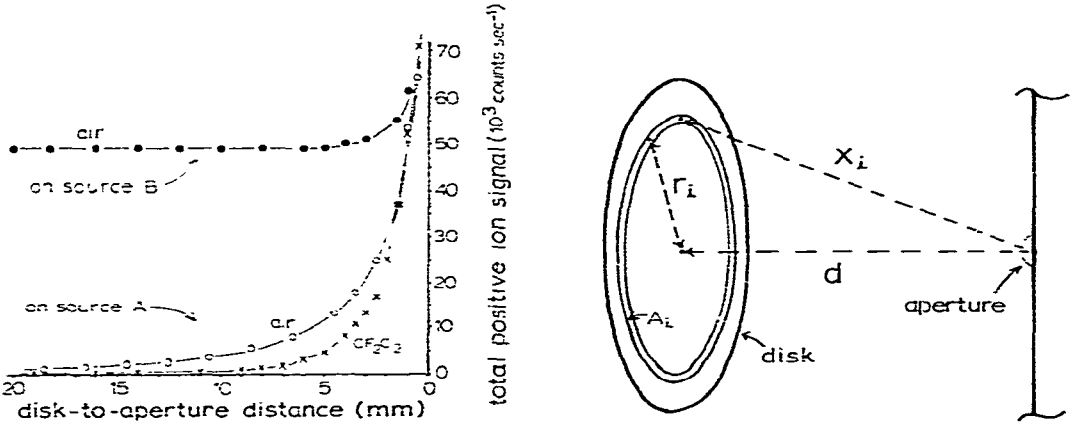


Fig. 2. Total positive-ion signals measured by mass spectrometer as a function of the disk-to-aperture distance. The source pressure and temperature are 0.85 atm and 23°C (ambient) in all cases.

Fig. 3. Representation of experiment using ion source A.

In order to develop a quantitative description of the data in Fig. 2 it is useful to consider the drawing in Fig. 3. In our experiment a signal is obtained which is proportional to the density of positive ions in a small region of space immediately adjacent to the aperture (signal = positive-ion density × flow-rate of gas through aperture × efficiency of ion transport through mass spectrometer). It is essential to the interpretation to be made here that the size of this volume being sampled by the mass spectrometer is small relative to the distances separating the $^{63}Ni$ disk and the aperture. We have given careful consideration to this point previously (p. 481 of ref. 4), and the conclusion is that the volume being effectively "seen" by the mass spectrometer is smaller than 0.5 mm, the distance of closest approach by the $^{63}Ni$ disk. The reason for this very local sampling of ion density by the mass spectrometer is that ions are rapidly destroyed in a field-free source by the recombination of opposite charge types. For ions which are formed more than 1 mm from the aperture, destruction by recombination is much faster than the rate at which they can be transported by gas flow to the aperture. Therefore, only ions which are formed very close to the aperture have a high probability of being measured by the mass spectrometer.

Again considering the drawing in Fig. 3, it is obvious that the ion density in the sampled volume will bear some type of inverse relation to the distance, $d$. Instead of

viewing the experiment in terms of the disk as a whole and the one value of $d$, however, it is useful to envision the disk as being composed of numerous concentric area units as shown, each having its own distance, $x_i$, to the aperture at each setting of $d$. The measured ion density will then be the result of a summation of contributions from the individual area elements of the disk. The very important advantage of viewing the experiment in this manner is that a generalized expression for the radiation intensity at the observation point will then result which, as will be seen, can then be used to predict the radiation intensity and ion density at any or all points in the active volume of any imagined cell design. Since we expect the contributions of each area unit, $A_i$, to the radiation intensity, $S$, at the observation point to be additive, eqn. 1 can be written

$$S = K \sum_i f(x_i) \tag{1}$$

where $K$ is a proportionality factor and $f(x_i)$ is some function (not yet determined) which describes the effect of separation, $x_i$, of each area unit on the radiation intensity at the observation point. Eqn. 1 assumes that the total emitter surface has been partitioned into individual units, $A_i$, of equal area. For the experiment symbolized by Fig. 3, the symmetry accompanying this cell design makes reduction of the system into equal area units with accompanying $x_i$ values very simple. In our calculations the disk was divided into twenty concentric rings of equal areas (rings are narrower as $r_i$ increases), and the value of $x_i$ associated with each is calculated from $x_i = (d^2 + r_i^2)^{1/2}$. With each setting of $d$, a unique combination of $x_i$ values are set, which should alter the radiation intensity and the positive ion density at the observation point in a manner consistent with eqn. 1. Viewing the problem in this way the critical remaining task is to determine the form of the function $f(x_i)$ which provides the best fit to the data.

In our initial attempts at matching the experimental data of Fig. 2 to a mathematical expression, several forms for $f(x_i)$ were somewhat arbitrarily selected for trial without much consideration being given to the physical basis of each. These attempts were not successful until, upon closer consideration of the theoretically expected form of $f(x_i)$, the following relationship between the mass spectrometry signal and the distances, $x_i$, was tested.

$$\text{signal} = K' \sqrt{\sum_i \frac{e^{-ax_i}}{x_i^2}} \tag{2}$$

where $K'$ is again simply a proportionality constant and $a$ is a constant which was adjusted to provide the best fit to the data. By inspection of eqns. 1 and 2 and realizing that the measured signal is proportional to positive-ion density, $n_+$, the following relationships are then also implied.

$$f(x_i) = \frac{e^{-ax_i}}{x_i^2} \tag{3}$$

and

$$n_+ \propto \sqrt{S} \tag{4}$$

Eqn. 2 appears to be a valid description of the experiment for the combined reasons that (1) it works and (2) it has a plausible physical basis (which will be related below). A demonstration of the fit of eqn. 2 to the experiments using air is shown in Fig. 4. For the moment, considering the data taken with source A, the solid curve shown is obtained by eqn. 2 where $a = 0.12\ mm^{-1}$. This calculated curve has been normalized to the data at the point where the measured signal is 10,000 counts/sec. The calculation is then seen to coincide with the other experimental points reasonably well. The dashed and dotted curves are calculations where the value of $a$ used is halved and doubled, respectively. These do not fit the data nearly as well. For the case of $CF_2Cl_2$ shown in Fig. 5, the solid line is again obtained from eqn. 2 but this time by using a value for $a$ of $0.50\ mm^{-1}$. It will be shown shortly in the discussion of the physical basis of eqn. 2, that the values of the constant, $a$, determined for air and $CF_2Cl_2$ in Figs. 4 and 5 have a definite physical meaning and could, in fact, have been predicted from independent measurements of a completely different type than those reported here.

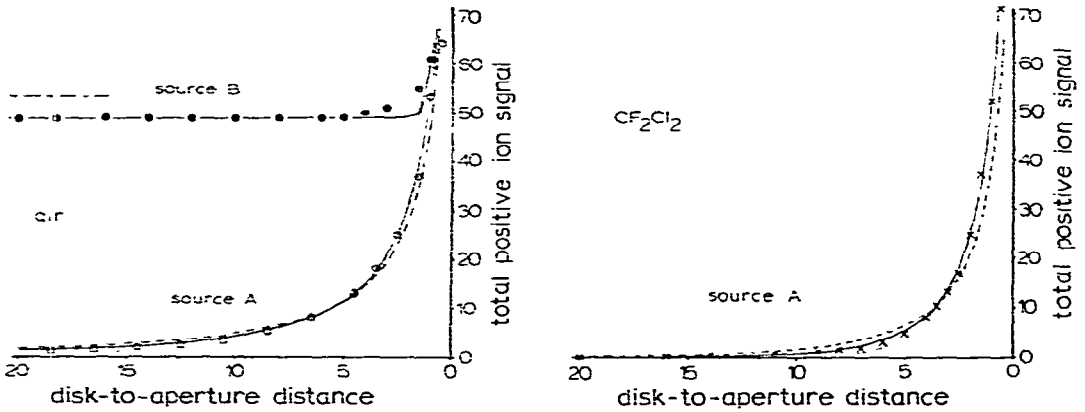


Fig. 4. Comparison of air data (dots and circles) with curves calculated from eqn. 2. For the source A curves the values of the coefficient $a$ used are: $a = 0.12\ mm^{-1}$ (solid), $a = 0.24\ mm^{-1}$ (dotted) and $a = 0.06\ mm^{-1}$ (dashed). All curves have been normalized with respect to the data at $d = 5.5$ mm, where the signal is 10,000 counts/sec. For the source B calculation, the solid curve is for $a = 0.12$ with normalization with respect to the source B data at $d = 20$ mm. The short dashed line is the calculated curve in this region, normalized with respect to the source A data at 5.5 mm.

Fig. 5. Comparison of $CF_2Cl_2$ data (X) with curves calculated from eqn. 2. The values of the coefficient, $a$, used for each curve are: $a = 0.50$ (solid), $a = 1.0$ (dotted), and $a = 0.25$ (dashed). The calculations have been normalized with respect to the data at $d = 3.5$ mm where the signal is 10,000 counts/sec.

The data in Fig. 4 where ion source B was used with air carrier gas can also be compared with a prediction based on eqn. 2. This is done with the solid curve (normalized to data point at $d = 20$ mm). To obtain this calculation the contribution to ionization at the aperture from the much larger cylindrical wall was also included by dividing the cylinder into a stack of rings, each having an area equal to each other and equal to the area of the individual units defined for the disk. As the disk is moved closer to the pin in source B, two opposing effects can be expected. Radiation intensity at the observation point will tend to be increased due to a closer disk, but also will tend to be decreased due to partial blockage of radiation from the wall by the disk. This "eclipse" of wall radiation should begin at *ca.* $d = 7.5$ mm and increase

continuously with closer approach of the disk. The solid line in Fig. 4, source B, was calculated with $a = 0.12\ \text{mm}^{-1}$. The prediction is that the mass spectrometry signal will change very little with $d$ until the last 2 mm of approach. The experimental data agrees reasonably well with this prediction, although the experimental points are observed to begin increasing measurably at *ca.* 4 mm, rather than at 2 mm. This difference is possibly due to the fact that the trajectories of betas in an attenuating medium are not necessarily straight and, therefore, the blockage of wall radiation by the disk is probably not quite as efficient as assumed in the calculation.

Just above the source B data in Fig. 4, a short dashed line is shown. This line indicates the predicted signal for source B if the calculations are normalized to the same reference point used for the source A calculation at $d = 5.5$ mm. The largest source of uncertainty in comparing the magnitudes of signals obtained by source A with those of source B results from the fact that upon changing the source a new aperture must be used. Our experience has indicated that each aperture causes a slightly different total ion signal to be observed, presumably due to slight variations in their sizes. Over the course of using about a dozen apertures in a given source, we estimate that the range of signal variations has been *ca.* 20%. Thus, it is seen that the total ion signal for source B is very adequately predicted by the source A data and eqn. 2.

*Physical justification for eqn. 2*

It can be shown that eqn. 2 has a physical basis from which the equation might have been suggested independent of our experiments. Furthermore it can be shown that even the correct value of the parameter, $a$, can be calculated from information readily available for the nuclide of interest.

We might start by explaining why $n_+$, the measured positive-ion density, is related to the square root of radiation intensity as stated directly in eqn. 4 and indirectly in eqn. 2. In a field-free ion source, ions are formed everywhere in the active volume in proportion to the radiation intensity, $S$, but are also rapidly destroyed by the recombination of the oppositely charged species. Very quickly equilibrium is established[5] and the rate of ion production equals the rate of ion loss by recombination. This is described by

$$\frac{dn_+}{dt} = 0 = \frac{S'}{V} - Rn_+n_- \tag{5}$$

where $S'$ is the ion-pair production rate in the observation volume, $V$, and is proportional to radiation intensity, $S$. $R$ is the positive ion–negative ion recombination rate. Since overall charge neutrality will be maintained at all points in this cell[5], $n_+ = n_-$, and eqn. 5 becomes

$$n_+ = \sqrt{\frac{S'}{VR}} \tag{6}$$

Thus, $n_+$ and the mass spectrometry signal should be proportional to the square root of the radiation intensity.

Having explained the square root portion of eqn. 2, we will next consider

whether eqn. 3, which expresses the critical form for $f(x_i)$, has a reasonable physical basis. The inverse square dependence on distance is to be expected to comprise a portion of $f(x_i)$ since this accounts for the well-known reduction in radiation intensity due to the effect of distance, alone, between a point source and the point of observation. It is not, however, as obvious why the simple function, $e^{-ax_i}$, should constitute the remainder of this function (unlike the usual visible light absorbance experiment in which monochromatic light is used, the beta radiation under consideration here consists of a wide range of energies). Nevertheless, the fact is that conventional nuclear measurements of beta emitters indicate that the attenuation of radiation intensity through a medium does, indeed, decrease linearly with the negative exponential of the absorbing mass density[6]. Taking a relevant example, the aluminum absorption curve for $^{63}$Ni-on-Pt foil has been reported by Brosi *et al.*[7]. In Fig. 1 of their report, a linear relationship exists between the logarithm of counts measured by a windowless Geiger–Müller counter and the mass per unit area of the aluminum foil which separates the $^{63}$Ni foil from the detector. (Since this is a parallel-plane experiment, no inverse distance squared component to the total relationship is expected or observed.) It is also important to note the magnitude of the absorption coefficient for $^{63}$Ni-on-Pt deduced by Brosi *et al.* They found that an aluminum foil of mass equal to 0.6 mg/cm$^2$ halves the radiation intensity detected. Expressing their results in the form $S/S_0 = e^{-aM}$, where $M$ is the mass per unit area (mg/cm$^2$) of the absorber, a value for $a$ equal to 1.15 cm$^2$/mg is obtained. In order to compare this value for $a$ expressed in units of cm$^2$/mg with the values of $a$ obtained from the experiments reported in this study, it is necessary to convert $a$ in the above expression to a form having units of thickness of a gaseous film. The density of a gas is given by the gas law, $D$ (mg/cm$^3$) = MW × $P/RT$. Multiplication of $D$ times $a$ (cm$^2$/mg) yields a value for $a$ in units of cm$^{-1}$. Conversion to units of mm$^{-1}$ yields $a$ (mm$^{-1}$) = 1.41 × MW × $P/T$, where MW, $P$ and $T$ are in units of g/mole, atm, and °K, respectively. With this conversion of units the equation which expresses the data of Brosi *et al.* becomes $S/S_0 = e^{-aX}$ where $X$ is the thickness of the absorbing gas (mm). If, instead of the parallel-plane experiment by Brosi *et al.*, the absorption of betas from $^{63}$Ni-on-Pt were measured using a point source emitter and a small area detector, the relationship between the measured radiation intensity and distance would be $S/S_0 = e^{-aX}/X^2$ where the value of $a$ is the same as in the parallel-plane experiment. The similarity of this function to eqn. 3 is encouraging and becomes even more so when the value of $a$ is predicted from the data of Brosi *et al.* As outlined above, their measurements indicate that $a$ (mm$^{-1}$) = 1.41 × MW × $P/T$. For the conditions used in our experiments shown in Figs. 2–4, $P$ = 0.85 atm and $T$ = 296°K. Therefore, for air (MW ≈ 29) and $CF_2Cl_2$ (MW = 121) $a$ values for these of 0.12 and 0.50, respectively, are predicted from independent experiments of a different nature than those described here. It will be recalled that these values are also the ones which gave the best fit to our measurements.

*Application to any $^{63}$Ni ionization cell*

One can now reliably predict that the relative radiation intensity anywhere in the active volume of a $^{63}$Ni-on-Pt ionization cell, will be given by

$$\text{rel } S = \sum_i \frac{e^{-ax_i}}{x_i^2} \tag{7}$$

and that the relative positive-ion density at any point in a field-free source will be given by

$$\text{rel } n_+ = \sqrt{\sum_i \frac{e^{-ax_i}}{x_i^2}} \tag{8}$$

where the summations are over all area units (of equal size) into which the total emitter is divided, and the value of $a$ is $1.41 \times \text{MW} \times P/T$.

Several example calculations are provided below for the $^{63}$Ni geometry most commonly used, the cylindrical cell. To relate the method by which this calculation has been done, consider the drawing shown in Fig. 6. The magnitude of $S$ or $n_+$ expected at any volume element, $V_r$, located anywhere within the active volume of this cylindrical cell, is calculated using eqn. 7 or 8. The main difficulty is determining the numerous values of $x_i$ separating each area unit, $A_i$, from the volume element, $V_r$. For the cylindrical cell these calculations are relatively straightforward if the cylinder is envisioned to be divided into a stack of rings and each ring is then divided into small rectangles (almost square) as shown in Fig. 6. The distance $x_i$ from each area unit to any point $V_r$ (located on a line crossing the cell and passing through its center) is obtainable by simple geometric calculations as shown. We have performed this calculation for a cylindrical cell of 10-mm diameter and 20-mm length. The cylinder is divided into 40 rings of 0.5-mm width and each ring is divided into 80 rectangles (defined by 360° of rotation about the center of a ring in increments of 4.5°). This cell then consists of 3200 area units. As each value of $x_i$ is found, its contribution to $S$ is added to that of the others according to eqn. 7. After completing all $A_i$ summations, another location for $V_r$ is chosen and the calculation is repeated. Using a handheld programmable calculator of modest capability (125 program steps were required), the magnitudes of $S$ and $n_+$ at all five non-repetitious points at 1-mm intervals along the cell diameter were produced by the calculator in *ca.* 1 h. This process was repeated for intervals of 2 mm along the length of the cell, starting at the middle and continuing to 10 mm past one end of the cell. The results of these calculations are shown in Fig. 7, where the value of $a$ chosen is 0.11. This choice for $a$ reflects, for example, the use of argon–methane carrier gas (MW$\approx$40) at 200°C. From calculations in Fig. 7, the relative magnitudes of $S$ and $n_+$ as a function of position across or along the cell are indicated. For example, at the center of this cell the positive-ion density will be 0.66 as great as the density 0.5 mm from the wall. The radiation intensity and ion-pair production rate in the center will be 0.44 as great as that 0.5 mm from the wall. (Due to the square root component of eqn. 8, the ion densities vary less with position than the radiation intensity values.) An interesting conclusion drawn from Fig. 7 is that in this field-free source, the relative ion density at positions well beyond the end of the cylinder remains surprisingly high; all along the cell cross-section at 10 mm from the end of the radioactive foil the ion density is about one-fifth (14/66) as great as at the center of the cell.

In order to demonstrate the effect of varied gas densities (which are determined experimentally by the choice of temperature, pressure, and molecular weight of the carrier gas) in the same 10-mm diameter cell, calculations were repeated using a range of $a$ values. The results of these calculations are summarized in Figs. 8–10, where different aspects of the ionization process are shown for all points (more

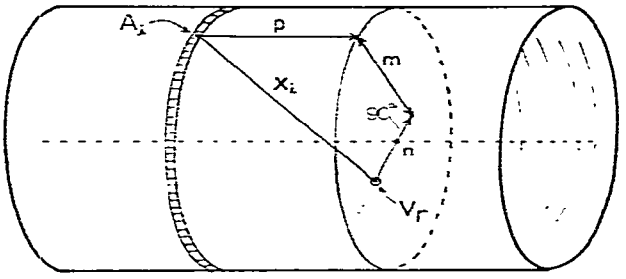


$$x_i = \sqrt{m^2 + n^2 + p^2}$$

Fig. 6. Representation of the method by which the distance, $x_i$, between any emitter area unit, $A_i$, and any volume element, $V_r$, of interest can be calculated. The observation element, $V_r$, must lie on a line running perpendicular to and passing through the axis of the cylinder.

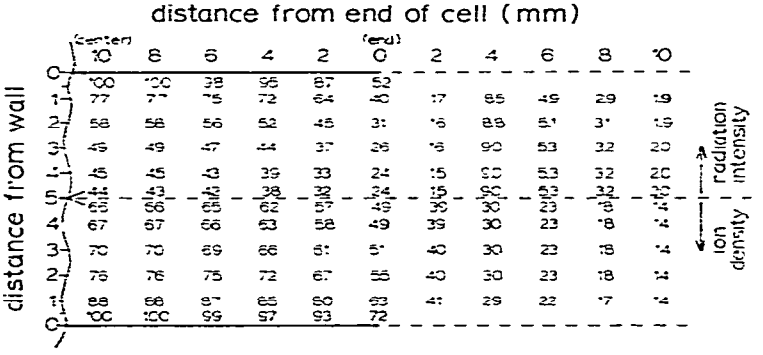


Fig. 7. Relative magnitudes of radiation intensities and ion densities predicted throughout the active volume of a $^{63}$Ni cylindrical source of 10-mm diameter and 20-mm length. Values are given at radial intervals of 1 mm and also at 0.5 mm from the cell walls. Values are given at longitudinal intervals of 2 mm and extend from the longitudinal center to 10 mm past the end of the cylinder.

than 0.5 mm from a wall) across the central diameter of the cell. Fig. 8 shows how radiation intensity varies with position and gas density. All curves have a common normalization point so that the magnitudes of the different curves are comparable with each other. Fig. 8 shows that the relative radiation intensity across the 10-mm cell with a $^{63}$Ni-on-Pt source is strongly dependent on the density of the carrier gas. In all cases the radiation intensity near the walls is greater than at the center. This data should not be taken to reflect the magnitude of relative ionization at each position, because the relative ion-production rate will be proportional to the product of radiation and density at each point. Therefore, in Fig. 9 the dependence of the relative ion-production rate on position is shown, where the production rate was obtained by multiplying the radiation intensity at each point by the value of $a$. Fig. 9 indicates that the production rate of ions at the center of the cell changes only moderately with variation of $a$ and passes through a maximum with $a \approx 0.2$ mm$^{-1}$. This maximum occurs because of the competition between gas density at the center and attenuation of radiation by intermediate layers of gas. Nearer the walls, however, the production rate is strongly dependent on gas density. It is important to point out here that the areas under each curve in Fig. 9 should provide a measure of the total ionization rate occurring throughout the cell. The maximum standing current expected for various

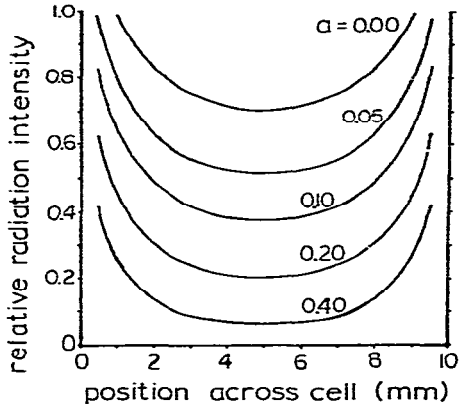


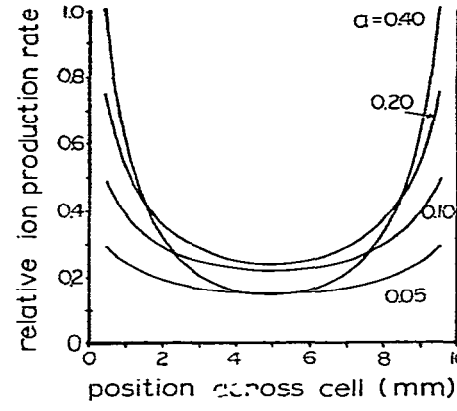


Fig. 8. Radiation intensity predicted across the center of a $^{63}$Ni cylindrical cell of 10-mm diameter and 20-mm length for selected values of the gas density coefficient, $a$.

Fig. 9. Ion-production rates predicted for cell described in Fig. 8.

conditions of temperature, pressure, and molecular weight of the carrier gas might thereby be predicted if this cell were an ECD.

In Fig. 10 the equilibrium ion densities in this same cell in the absence of all electric fields are shown as a function of gas density. As in Fig. 7 these do not vary with position as strongly as do the ion-production rates. Normal conditions within a typical ECD are perhaps best represented by the $a = 0.1$ curve. For this gas density, the ion densities shown vary by only *ca.* 25% across the interior 9 mm of the cell's diameter. If high pressures (such as 4 atm) or high molecular weight carrier gases are used in this cell, ion densities will then become much more dependent on position within the cell. Fig. 10 should be applied to experimental conditions with caution since under typical conditions of the ECD, for example, electric fields are applied.

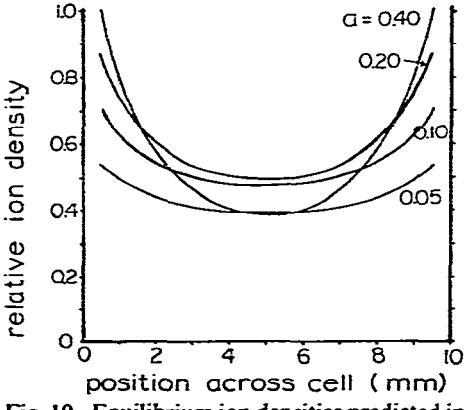


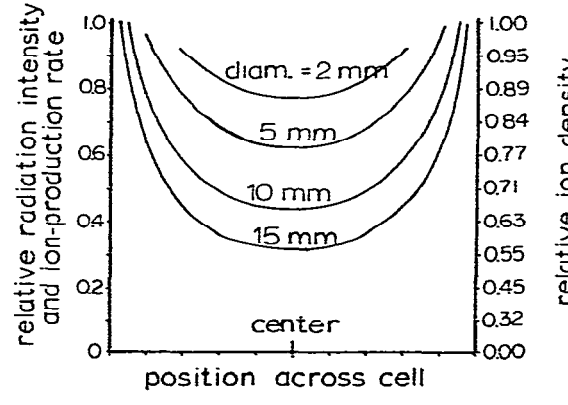


Fig. 10. Equilibrium ion densities predicted in the cell described in Fig. 8 if the cell is free of applied electric fields.

Fig. 11. Predicted effects of size of $^{63}$Ni cylindrical cells on relative radiation intensity, ion-production rate and equilibrium ion density. For all cells the length is assumed to be twice the diameter. The calculations apply to positions across the longitudinal center. A gas density coefficient of $a = 0.11$ has been used.

The complete discription of ion distributions in these cases must also take into account the applied field, the resulting space–charge fields due to the separation of charge types, and the migration of electrons and ions in these fields. For the pulsed ECD we have previously done this, starting with the assumption that the ionization rate is equal everywhere in the active volume[3].

In Fig. 11, the effect of the size of the cylindrical cell is shown. Relative radiation intensity and relative ion production can now be expressed together because only one gas density ($a=0.11$) is considered. All curves terminate at a position 0.5 mm from the cell wall. Again, these calculations are all mutually comparable. Therefore it is seen that the radiation intensity, the ion-production rate and the relative ion density at the center of these cells are greatest for the smallest cell, even though the total activity of this cell will be only 1/56 as great as that of the largest cell.

## CONCLUSION

We have described here a method by which ionization parameters of any imagined $^{63}$Ni-on-Pt ionization cell might be calculated. The method should also be applicable to ion sources which use other beta-emitting nuclides as long as the mass absorption curve of that nuclide has been measured. With other nuclides the only alteration in the calculations described here will be in the coefficient, $B$, in the general expression, $a = B \times \mathrm{MW} \times P/T$.

There are a multitude of previous reports concerning the ECD, APIMS, and IMS which could be compared with the observations and predictions related in this paper. We will certainly not attempt such an ambitious task here. We will, however, comment briefly on the compatibility of our results with those of the two recent studies[1,2] referred to in the Introduction.

Aue and Kapila[1] measured direct currents in a $^{63}$Ni ionization cell, where the $^{63}$Ni was in the form of a small disk and was moveable relative to the counter electrode. At ambient pressure and temperatures in nitrogen gas their measurements indicated that the "center of ionization" occurs at a distance of *ca.* 1 mm from the foil. The ionization cell they used is very similar to our ion source A. Therefore, in the experiment shown in Fig. 12, in which the d.c. cell current of source A has been

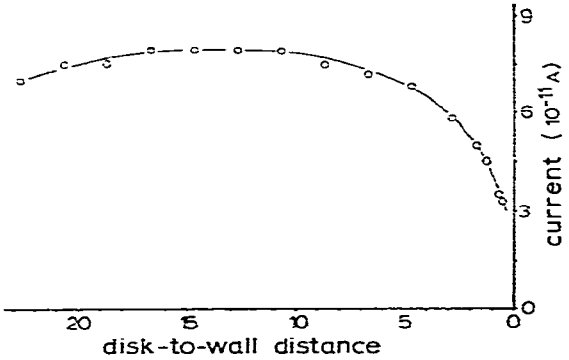


Fig. 12. Cell current measured with source A with nitrogen carrier gas at ambient temperature and pressure as a function of disk placement. This is a d.c. measurement where the pin is positively polarized by connecting a 50-V battery between the moveable pin and the electrometer.

measured as a function of distance, $d$, a result similar to that of Aue and Kapila might be expected. It is seen in Fig. 12 that the value of $d$ at which the measured current decreases to 50% of the maximum value does, indeed, occur at *ca.* $d = 1$ mm. Therefore, in our source, also, the "center of ionization" *for this source geometry* appears to be *ca.* 1 mm from the disk surface. Also, if one considers the mass spectrometry data from the disk experiment in air shown in Fig. 4, the experimental points and the solid curve are seen to be rising rapidly at $d = 1$ mm. Furthermore, the solid curve is for $n_+$, whereas to compare with a d.c. measurement a curve for ion-production rate would be more appropriate. Since ion-production rate is proportional to the square of $n_+$, that curve would be rising even more rapidly in the vicinity of $d = 1$ mm. From the ion measurements, also, it then seems reasonable that the "center of ionization" *for this cell design* under these conditions occurs at *ca.* 1 mm from the foil. We hasten to add, however, that this value for the "center of ionization" should be applied to other cell designs only with caution. In the experiments just described, the fall-off of radiation with distance from the foil will be reduced by some type of $1/d^2$ component (as well as the absorption component) which will be determined by the exact size of the disk. (The small-disk experiment represents neither a true parallel-plane nor point-source design, but is a composite of the two.) Recognizing this, the data of Ayala *et al.*[2] can be viewed as being consistent with and not contradictory to that of Aue and Kapila. Ayala *et al.* found that, with a cell of cylindrical geometry and a diameter of 14 mm, the ion-pair production rate increases continuously with carrier gas density (their Fig. 7). The increase in production rate with $P/T$ is somewhat less than a proportional relation at ambient values of $P/T$, and the dependence becomes progressively weaker at high values of $P/T$. This result seems to indicate that a major portion of the $^{63}$Ni betas at STP conditions of argon–methane carrier gas penetrate completely across their 14-mm cell. While this may appear inconsistent with the small-disk experiment, it can be shown that there actually is no contradiction when the total systems are considered. The calculations discussed above which supported the measurements of Aue and Kapila also lead to Fig. 9. From the data in Fig. 9, an estimate of the dependence of the ion-production rate on the gas density can be obtained by comparing the relative areas under each curve. For this 10-mm cell, it is seen that an increase in density above ambient levels (*ca.* $a = 0.1$) is expected to result in an increase in the ion-production rate. As the gas density is increased to relatively large values, an accompanying increase in production rate should continue but this dependence should become progressively weaker, as was observed by Ayala *et al.* Thus, the apparent differences between these two reports are resolved by the view provided here and are seen to result primarily from the different source geometries studied rather than the nature of $^{63}$Ni beta penetration.

The objective of this study has been to describe the ionization processes occurring everywhere within the active volume of an ion source. Other parameters of general interest, such as total charge production rate, should be obtainable from these by integration over the entire volume. The results reported here and the method developed for describing any imagined beta ionization cell should be useful for future uses and studies of these devices.

ACKNOWLEDGEMENTS

This work was supported by grant number CHE-7824515 from the National Science Foundation. The authors are also indebted to Reed Howald for numerous helpful discussions.

REFERENCES

1 W. A. Aue and S. Kapila, *J. Chromatogr.*, 188 (1980) 1.
2 J. A. Ayala, W. E. Wentworth and E. C. M. Chen, *J. Chromatogr.*, 195 (1980) 1.
3 E. P. Grimsrud, S. H. Kim and P. L. Gobby, *Anal. Chem.*, 51 (1979) 223.
4 P. L. Gobby, E. P. Grimsrud and S. W. Warden, *Anal. Chem.*, 52 (1980) 473.
5 M. W. Siegel and M. C. McKeown, *J. Chromatogr.*, 122 (1976) 397.
6 G. D. Chase and J. L. Rabinowitz, *Principles of Radioisotope Methodology*, Burgess Publishing, Minneapolis, MN, 1959, p. 123.
7 A. R. Brosi, C. J. Borkowski, E. E. Conn and J. C. Griess, Jr., *Phys. Rev.*, 81 (1951) 391.